Typical auroral substorm: A bifurcated oval

J. W. Gjerloev,[1] R. A. Hoffman,[2] J. B. Sigwarth,[3] L. A. Frank,[4] and J. B. H. Baker[1]

Received 29 March 2007; revised 16 October 2007; accepted 16 November 2007; published 28 March 2008.

[1] Utilizing global auroral images obtained by Polar Visible Imaging System Earth Camera, we have analyzed the UV emissions from 116 auroral substorms. The events selected were fairly isolated and had to expand from a localized onset. It was found that essentially all auroral events fulfilling these simple criteria expand into the Akasofu (1964) bulge-type aurora. Averaged auroral emission patterns were compiled for 11 time steps of the substorm covering 20 min prior to the onset until well into the recovery phase. This compilation required a three-step normalization technique, one temporal based on the expansion time and two spatial, magnetic local time and latitude. These average patterns were then fit to either a single or double Gaussian distribution in latitude for each of 24 magnetic local times. On the basis of this analysis we made the following conclusions. The normalization technique is highly efficient in maintaining the key features in the individual auroral emission patterns, even though the individual events varied significantly in intensity, size, position, and lifetime. Thus our normalization results quantitatively validate the Akasofu (1964) assumption that key auroral features exist in the bulge-type auroral substorm. After the substorm onset the auroral oval becomes clearly bifurcated consisting of two components: the oval aurora in the latitude range of the preonset oval and expanding primarily eastward postmidnight, and the bulge aurora, which emerges out of the oval, expanding poleward and both east and west in MLT. The oval aurora decay faster than the bulge emissions indicating that the decays have separate time constants. Owing to the pronounced difference in the spatiotemporal behavior of the two auroral components we suggest that their sources are quasi-independent.

Citation: Gjerloev, J. W., R. A. Hoffman, J. B. Sigwarth, L. A. Frank, and J. B. H. Baker (2008), Typical auroral substorm: A bifurcated oval, *J. Geophys. Res.*, *113*, A03211, doi:10.1029/2007JA012431.

1. Introduction

[2] The groundbreaking phenomenological substorm study by *Akasofu* [1964] still serves as a reference frame for the auroral substorm, which is the most common type of large-scale auroral disturbances. Subsequently, a large number of event studies have investigated various aspects of the auroral substorm, but only a few studies have attempted to quantify the spatiotemporal behavior of the auroral oval specifically during substorms. In fact, to date there is still no quantitative description of the classical global Akasofu-type substorm beyond the initial diagrams. This is rather remarkable considering the massive amount of high quality global auroral images obtained by space borne imagers. In questioning what a substorm looks like, the consensus has been to adopt the Akasofu diagrams. What is missing is a superimposed epoch analysis of the auroral substorm that can quantitatively describe the growth, brightening, and decay of the auroral substorm. To address this shortcoming, we adopt the same fundamental assumption of Akasofu that auroral substorms have a characteristic temporal behavior and display primary characteristics that are common to all events. In this paper we will justify this approach and show that with the correct types of normalization we can perform a superimposed epoch analysis while minimizing the smearing of key auroral characteristics.

[3] In the description of the Dynamics Explorer 1 spin scan photometer, *Frank et al.* [1981] wrote "...imaging will provide a natural coordinate system, and a monitor of magnetospheric and ionospheric activity, to reference in situ point measurements with both spacecraft and thus allow truly global analyses...." This interesting idea is clearly consistent with the above-mentioned Akasofu assumption and implies that the auroral electrodynamic parameters are organized by the optical emissions rather than any fixed coordinate system such as the much used magnetic local time (MLT)–invariant latitude (ILat) system. Neither Akasofu nor *Frank et al.* [1981], however, provided a quantitative justification of the assumption. This was not done until *Fujii et al.* [1994] developed a unique technique to analyze auroral electrodynamics during substorms. From a set of Dynamics Explorer 1 (DE-1) global auroral images

[1]Johns Hopkins University Applied Physics Laboratory, Laurel, Maryland, USA.
[2]Space Weather Laboratory, NASA Goddard Space Flight Center, Greenbelt, Maryland, USA.
[3]Division Office, Heliosphysics Division, NASA Goddard Space Flight Center, Greenbelt, Maryland, USA.
[4]Department of Physics and Astronomy, University of Iowa, Iowa City, Iowa, USA.

Copyright 2008 by the American Geophysical Union.
0148-0227/08/2007JA012431

they defined a generic bulge-type auroral substorm (a typical emission pattern) onto which simultaneous low altitude DE-2 auroral oval crossings were positioned with respect to key features in the emission pattern. This allowed them to organize the DE-2 electrodynamic data with respect to the generic aurora, instead of using MLT as typically had been done.

[4] Then *Gjerloev and Hoffman* [2000a, Figure 2] showed that using MLT alone to organize data will unavoidably lead to smearing of the electrodynamic parameter in question. Of interest to this paper, *Gjerloev and Hoffman* [2000b] took the normalization technique one step further by normalizing the latitudinal width using the measured electron precipitation. *Newell et al.* [2001] used Polar UVI images in a superposed epoch study of a large number of substorms. They organized the data in time by the auroral onset as determined from the images but no spatial organization was used. This approach did not take into account the known variation in the position of key emission features such as the onset itself [e.g., *Gjerloev et al.*, 2007; *Frey et al.*, 2004; *Craven and Frank*, 1991]. Recently, *Mende et al.* [2003] have presented an interesting superposed epoch study based on data from the Wideband Imaging Camera and the Spectrographic Imager carried on the Image satellite. Data were organized in time from the auroral onset and in local time by their distance in MLT from the auroral onset. Finally, *Gjerloev et al.* [2007] analyzed the spatial and temporal expansion of the bulge-type auroral substorm by manually selecting the locations of key points in the UV global optical patterns of 116 events and statistically obtaining the average positions and expansion speeds of these points. They normalized substorm time based on the time from onset to maximum expansion. Their study represented the first quantification of the Akasofu diagrams.

[5] In this paper we will address the spatiotemporal behavior of the UV auroral oval and show quantitatively that the basic assumption of *Akasofu* [1964] is valid during auroral substorms that expand out of a localized onset. *Gjerloev et al.* [2007] performed a manual identification of key emission features and their temporal behavior was determined. For example, they quantified the location of the bulge aurora and its expansion out from the initial onset location. The current paper develops and validates a new normalization technique and utilizes it to determine average global emission patterns. There is no overlap with the *Gjerloev et al.* [2007] paper although the results are found to be in agreement. The technique used here is automated with a poleward and equatorward boundary determination scheme, resulting in the ability to place a pixel or map any type of measurement onto a spatially and temporally normalized substorm optical pattern. Section 2 will describe the data utilized and section 3 explains the event selection criteria, which is the same set used by *Gjerloev et al.* [2007]. Section 4 describes the normalization technique, which together with the results of the boundary determinations allowed the derivation of the normalized substorm optical patterns as a function of substorm time. The method is then validated in section 5. Section 6 is an analysis of the average substorm emission patterns as a function of substorm time, and section 7 is a discussion of our results with a focus on a new and important finding: the apparent bifurcation of the auroral oval during both the expansion and recovery of a substorm. Finally, section 8 summarizes the combined principal results from the analyses of the average substorm patterns performed in this paper as well as the statistical study of the same substorm set by *Gjerloev et al.* [2007].

2. Data

[6] The primary dataset for this study comes from the Earth camera images acquired by the Visible Imaging System (VIS) on the Polar satellite [*Frank et al.*, 1995]. This camera provides global auroral images in the vacuum ultraviolet (VUV) in contrast to the more limited views but higher spatial resolution from its two visible imaging cameras. The VUV image repetition rate was 1 to 5 min depending upon whether the Earth camera was sharing the VIS telemetry allocation with the visible imagers. To ensure an onset timing with a precision of about 1 min, the Earth camera data were often supplemented with images from the visible imaging cameras and the image data from the Ultraviolet Imager (UVI) on Polar [*Torr et al.*, 1995]. The combination of these data sets also enabled the elimination of pseudo onsets and ensured that the substorm developed continuously out of the identified onset. (See *Gjerloev et al.* [2007] for further discussion.)

3. Event Selection

[7] The selection of an event to be included in this statistical study is identical to that used by *Gjerloev et al.* [2007] and is based both on its optical characteristic and the AL index pattern around the time of the event. All available ground-based magnetometer stations (>100) were used to deduce AL and AU. The criteria used are (1) isolated single event optically and magnetically; (2) poleward expansion from a localized onset; (3) single expansion and recovery phase (in case of a secondary expansion the event end is defined as the time of the second expansion); (4) entire auroral bulge in darkness and viewed by the imager; (5) image aspect adequate to make measurements on expanded emission region; (6) not during magnetic storms ($|Dst| < 30$ nT) or periods of long magnetic activity.

[8] The requirement of a localized onset in the nighttime hours eliminates the shock or pressure pulse auroras [*Zhou et al.*, 2003] and the crescent aurora [*Gjerloev et al.*, 2000c], since the former originates on the dayside and is propagated along the auroral oval to the nightside, while the latter is a nearly simultaneous brightening along a large portion of the nightside oval. The darkness requirement ensures that the observed auroral emissions are due to particle precipitation, eliminates any terminator effects, and allows the high- and low-latitude boundaries of the aurora to be unambiguously determined with no sunlight contamination. Darkness is defined in this study as any pixel with a solar zenith angle greater than 97 deg. Finally, we require that the entire poleward expanding bulge is visible in the VIS images.

[9] On the basis of these criteria, we selected 116 events from the years 1997 to 2001 when the Polar imaging was most advantageous. The events are clustered around winter solstice due to the darkness requirement. Since there were no criteria used pertaining to the characteristics of the expansion of the optical emissions beyond expansion from

a localized region, some rather unusually looking events were kept in the database. However, we found that essentially all of these selected events expanded into the *Akasofu* [1964] bulge-type auroral substorm.

4. Method

[10] In this section we will explain the motivation for our approach, the normalization technique used, and an application to determine an average UV emission pattern as a function of substorm time.

4.1. Motivation

[11] In the phenomenological model by *Akasofu* [1964] the auroral oval was illustrated to be highly variable in time and space. This variability raises the fundamental question: How can the major characteristics of individual events be maintained in a statistical average model? Figures 1a and 1b show two examples of auroral events near the maximum intensity with superposed boundaries determined by an automated routine (see section 4.4). The remaining panels will be discussed later in the paper. A few common features should be identified: a poleward expanded oval resulting in a nearly straight-line poleward boundary, a surge brightening, and a large fattening of the auroral oval to the east of the surge also containing a region of enhanced emissions. However, a few major differences should also be noted. The local time region and extent of the auroral brightening's are different, the latitudinal width and position of the auroral oval are different, and finally the intensity as seen by the images is clearly different. In deriving a statistical model, the challenge is to maintain the common characteristic features of the individual events despite the differences.

[12] While the intensity difference does not affect the spatial characteristics of the substorm we must carefully address those factors that complicate the derivation of a statistical average model: (1) The wide range in temporal evolution of auroral substorms from 5 min to some tens of minutes to several hours [*Gjerloev et al.*, 2007; *Pellinen et al.*, 1994; *Weimer*, 1994; *Chua et al.*, 2004]; (2) the variation in local time position of auroral features from event to event, for example the MLT variation (full width at half-maximum, FWHM, of 3.0 h) in the location of the head of the surge at the peak of the substorm [*Gjerloev et al.*, 2007, and references therein]; and (3) the high variability in the extent of the poleward expansion [e.g., *Gjerloev et al.*, 2007]. To derive our model, we have employed a three-step normalization process: (1) normalize the timescale of the substorm; (2) normalize the local time extent and position of the auroral bulge; (3) normalize the latitudinal extent and position of the auroral oval.

4.2. Normalize Substorm Time

[13] We normalize the substorm time (using the approach of *Gjerloev et al.* [2007]) by defining the onset of brightening as T = 0.0 and peak of the substorm as T = 1.0. Our selection of these times is based purely on the global auroral images. Utilizing the Polar VIS Earth Camera and the Polar UVI enables us to determine the onset time to within 1 min which is sufficient accuracy for our study. Our substorm maximum or end of the expansion phase is based on a qualitative estimate of the combined intensity of the event and the westward and poleward expansion of the poleward auroral boundary. We often found that the intensity begins to fade before the expansion ceases, especially at the ends of the bulge [*Gjerloev et al.*, 2007]. Thus our selection provides a more integrated optical characteristic to the global aurora in the selection of the maximum than using either parameter alone. Our optical analysis gives an average substorm expansion phase of about 30 min. The normalized time steps used for each event during the expansion phase are T = 0.0, T = 0.5, T = 1.0. During the recovery phase we continue to use the normalized timescale at times T = 1.5, 2.0, 2.5, and 3.0. This contrasts to the work of *Chua et al.* [2004]. They used an approximation for hemispheric power computed from the Polar UVI observations to calculate an exponential decay time constant independently from the expansion phase time for each of over 300 substorm events. While they found differences in the mean times for expansion and decay, both values were around 30 min, comparable to our average expansion time and time from maximum to T = 2.0. This lends credence to our continuing use of the average expansion phase time constant during the recovery phase. Interestingly, their use of a single decay constant implies that the substorm consist of a single system an assumption we will question later in the paper. Prior to the event (growth phase) we use minutes prior to onset: T = −20 min, T = −15 min, T = −10 min, and T = −5 min. Thus in total we divide the substorm into 11 time steps.

4.3. Normalize Local Time

[14] The second step in the normalization scheme eliminates the varying local time position of the auroral bulge. We use the MLT position of the head of the surge (*HS*) and the east end of the bulge (*EB*) from the *Gjerloev et al.* [2007] database. The red lines in Figures 1a and 1b indicate the identified MLT position of these boundaries.

[15] Average positions of the head of the surge ($\overline{HS}$) and east end of the bulge ($\overline{EB}$) are calculated from all 116 events and the local time is divided into three sectors: (1) from magnetic noon (*MN*) to *HS*; (2) from *HS* to *EB*; (3) from *EB* to *MN*. Let us assume that a pixel *P*(*MLT*, *ILat*) is located within the bulge local time sector. The normalized local time position (MLT') of that pixel is straightforwardly determined as

$$MLT' = \overline{HS} + \left(\overline{EB} - \overline{HS}\right) \cdot (MLT - HS)/(EB - HS) \qquad (1)$$

[16] Listed in Table 1 are the values of $\overline{HS}$ and $\overline{EB}$ with the FWHM of the distribution of locations. (See *Gjerloev et al.*, 2007, for histograms of the distributions of these points.) The large spread in locations (see FWHM in parenthesis) indicates the need for this normalization to avoid smearing the surge over MLT and smearing the length of the bulge. This procedure will change the local time length of each auroral bulge to the average bulge length as well as position each pixel of each bulge within the average bulge. Naturally, if the pixel were located in one of the other two local time sectors the normalization would be performed using equation (1) with appropriate changes to sector boundaries.

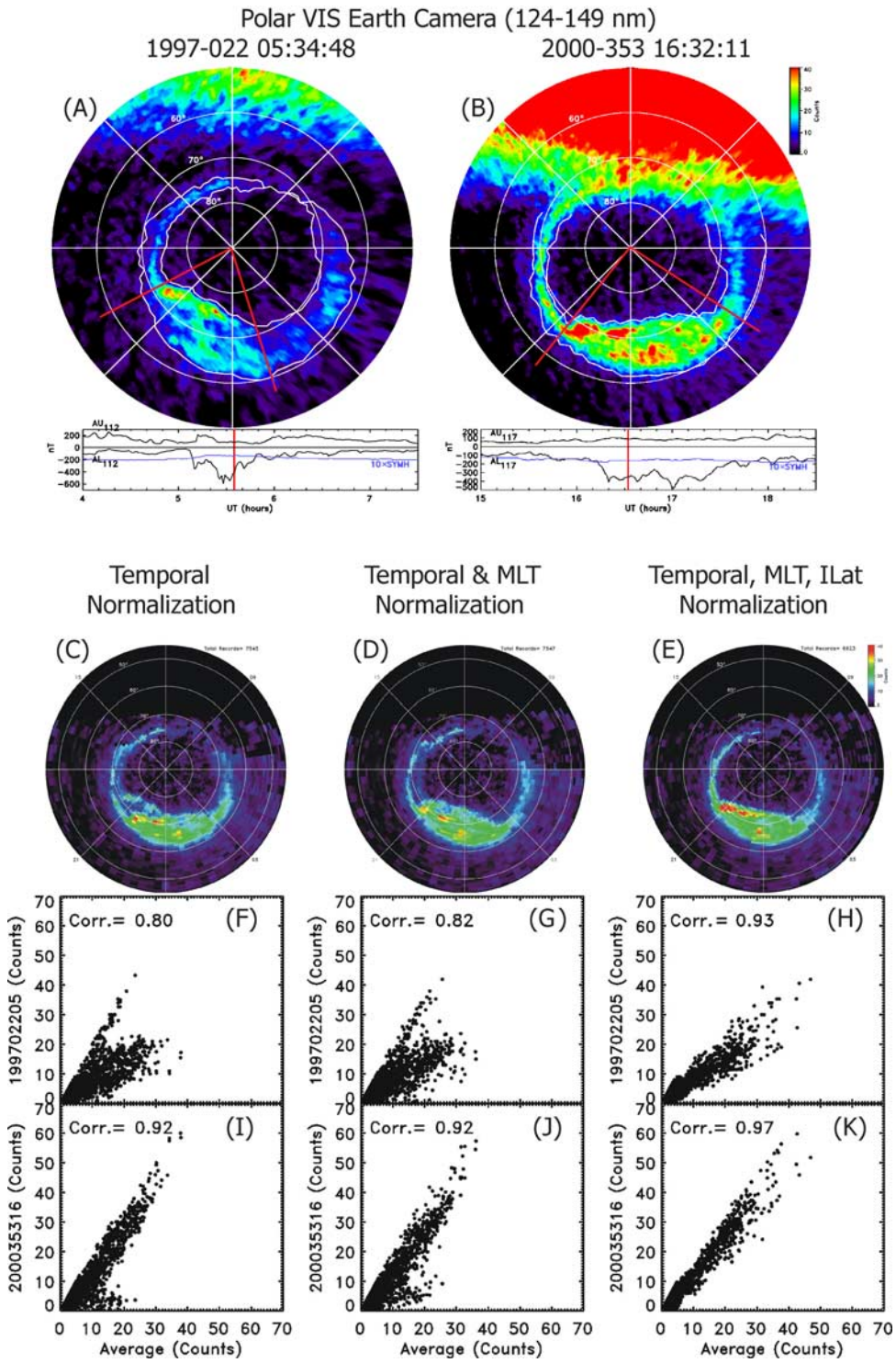

Figure 1. (a and b) Polar Visible Imaging System (VIS) Earth Camera images near the peak of two classical substorms with *AE* indices. The red lines on the images indicate MLT boundaries of the poleward expansion while the vertical lines on the *AE* plots indicate times of images. Also shown are (c–e) average patterns of the two images using three different levels of normalization and (f–k) the results from a correlation analysis of images and the average patterns (see text for detail).

4.4. Normalize Latitude

[17] The third and final step eliminates the varying latitudinal location and width of the auroral oval. This is done in a similar way to the above MLT normalization although it requires a nontrivial determination of the low- and high-latitude auroral boundary. These boundaries are determined by a software package that was developed for the purpose. The technique differs from the widely used

Table 1. Average Head of the Surge ($\overline{HS}$) and East End of the Bulge ($\overline{EB}$) Positions for the Various Stages of the Substorm[a]

Time Stamp	$\overline{HS}$	$\overline{EB}$
T = −20 min	22.4 (2.8)	22.4 (2.8)
T = −15 min	22.4 (2.8)	22.4 (2.8)
T = −10 min	22.4 (2.8)	22.4 (2.8)
T = −5 min	22.4 (2.8)	22.4 (2.8)
T = 0.0	22.4 (2.8)	22.4 (2.8)
T = 0.5	21.0 (3.1)	1.5 (3.2)
T = 1.0	20.5 (2.7)	2.5 (2.4)
T = 1.5	20.1 (3.5)	2.9 (3.2)
T = 2.0	20.1 (3.3)	3.0 (2.8)
T = 2.5	20.3 (3.1)	3.1 (2.4)
T = 3.0	20.4 (3.1)	3.2 (2.4)

[a]Note that at onset and during growth phase we use $\overline{HS} \equiv \overline{EB}$ (see text). In parenthesis is shown the FWHM of the Gaussian distribution (from *Gjerloev et al.* [2007]).

method published by *Craven and Frank* [1991] and *Brittnacher et al.* [1999] which used a fixed threshold to eliminate pixels and subsequently find oval boundaries (also see *Germany et al.* [1998] for a neural network approach). Our method is based on the local statistics of the particular image. There is no fixed threshold, no smoothing in time, and all images are analyzed individually. After a polar projection of the image using an AACGM latitude–magnetic local time coordinate system, we determine 90 latitudinal cuts (4 degrees longitudinal separation) from the pole to 30 deg with a resolution of 0.5 deg in latitude. For each of these cuts the poleward and equatorward boundaries are determined. A weighted smoothing of the two sets of 90 boundary positions provides the final boundaries.

[18] The boundaries for the individual cuts are determined in three steps (here only explained for the poleward boundary).

[19] 1. For each local time cut the local intensity maximum is obtained within the latitude range of an assumed oval. The initial poleward boundary is then defined as the first pixel poleward of the maximum with a value of 0 counts.

[20] 2. For each local time cut a threshold value is determined as the sum of the average and standard deviation of the pixels located poleward of this initial boundary. The poleward boundary is then redefined as the first pixel poleward of the maximum with a value smaller than the threshold.

[21] 3. If any pixels poleward of the boundary exceed the threshold we evaluate the significance of such a spike. The significance is determined from the average count of the pixels within the spike exceeding the threshold and the distance in degrees from the poleward boundary. The significance of the spike decreases with increasing distance to the oval and the significance decreases with a decrease in the average counts of the spike.

[22] It should be noted here that the method is fully automated, does not involve any fixed threshold, and requires no subjective adjustment for any of the >1200 images analyzed. Examples of the automated boundaries can be seen in Figures 1a and 1b. Figure 2 shows superposed boundaries for all 116 events for three time steps with the average boundaries superposed in black. Note the large spread in the locations of the individual boundaries, indicating the necessity of this normalization. Also note that the average poleward boundary across the bulge is a reasonably straight line, rather than aligned with constant magnetic latitude, maintaining one of the characteristics seen in the two examples in Figure 1. Figure 3 shows these average boundaries with standard deviations indicated for all 11 time steps.

[23] The ILat position of the poleward boundary (PB) and equatorward boundary (EB) are obviously a function of MLT such that $PB = PB(MLT)$ and $EB = EB(MLT)$. The positions of these boundaries must be determined in the normalized MLT system following the above normalization scheme thereby providing $PB(MLT')$ and $EB(MLT')$. First, average oval boundaries ($\overline{PB}(MLT')$) and ($\overline{EB}(MLT')$) are calculated from all 116 events (see Figure 2). Then the latitude is divided into three sectors: (1) from magnetic pole to $PB(MLT)$; (2) from $PB(MLT)$ to $EB(MLT)$; (3) from $EB(MLT)$ to magnetic equator. If the above-mentioned pixel $P(MLT, ILat)$ is located within the oval, we can now determine the latitudinal position of that pixel within the normalized bulge $P(MLT', ILat')$ as:

$$ILat' = \overline{EB}(MLT') + \left(\overline{PB}(MLT') - \overline{EB}(MLT')\right) \cdot (ILat - EB(MLT'))/(PB(MLT') - EB(MLT')) \quad (2)$$

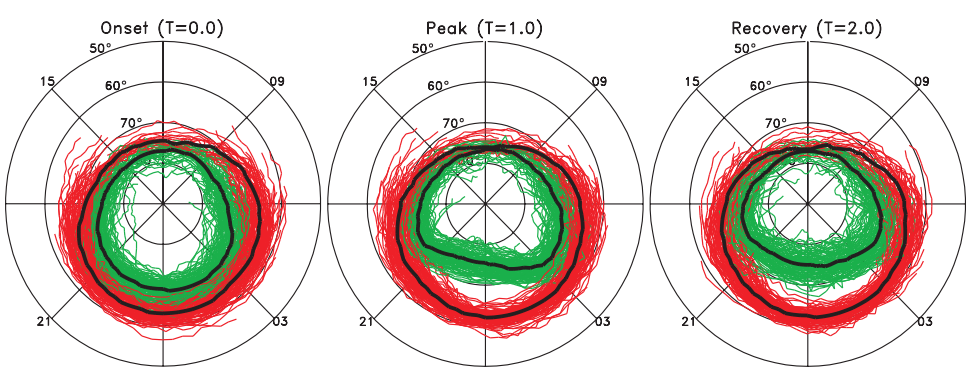

Figure 2. Automated determination of auroral oval boundaries for 116 events. Green and red show the high-latitude and low-latitude boundaries, respectively, while the black lines are the average locations. The three normalized time steps T = 0.0, T = 1.0 and T = 2.0 are shown. See text for explanation of the normalized timescale.

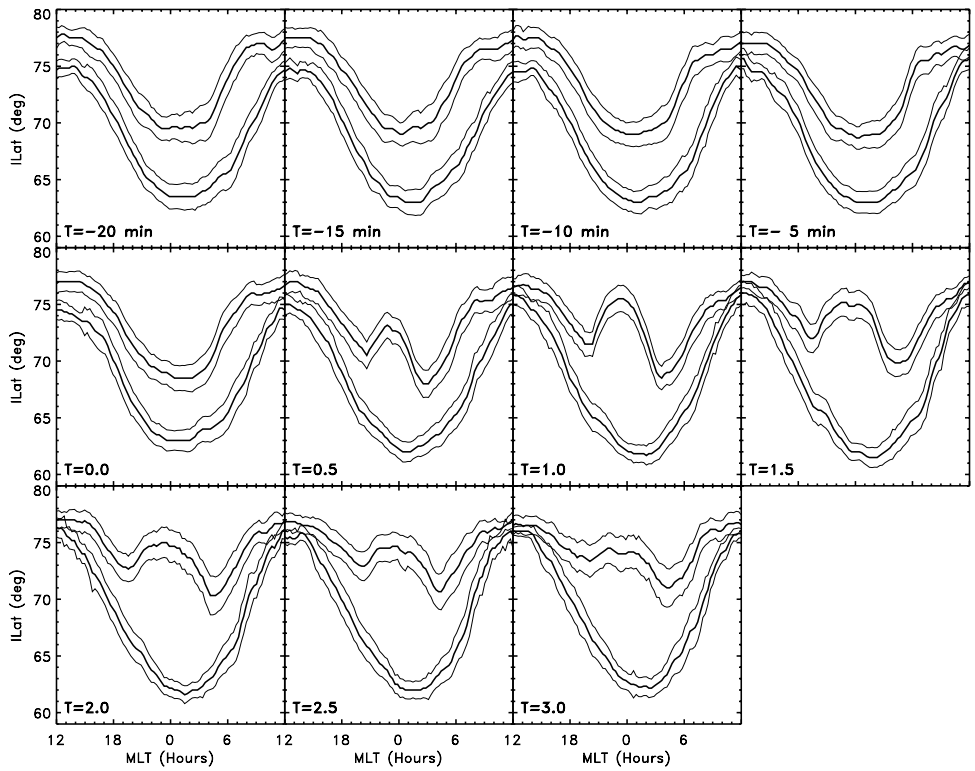

Figure 3. Average oval boundaries (thick lines) are shown for each of the 11 substorm time steps. Also indicated is the standard deviation (thin lines).

where MLT' is determined by equation (1). If the pixel is located in one of the other two latitudinal sectors the local time normalization is performed using equation (2) with appropriate changes to the sector boundaries. Since we are only concerned with the averages for the remainder of the paper, we will ignore the primed notation. We can express these average oval boundaries as a function of MLT as seen in Figure 2 in a convenient form by the use of a simple truncated Fourier series:

$$Ilat(MLT) = H_0^R + \sum_{n=1}^{NC-1} \left\{ H_n^R \cos(n \cdot MLT \cdot \pi/12) + H_n^I \sin(n \cdot MLT \cdot \pi/12) \right\} \quad (3)$$

where the coefficients $H_n^{R,I}$ are given by Tables 2 and 3 and NC is the cutoff frequency. NC is chosen as the minimum number of coefficients fulfilling the requirement:

$$\max(abs(fit - data)) + \sigma < 1 \quad (4)$$

where σ is the standard deviation between the fit and data. Hence we require that no single point deviates more than 1° minus the standard deviation. It should be mentioned that *Holzworth and Meng* [1975] used a similar technique to determine simplified fits to the statistical *Feldstein* [1963] auroral ovals and DMSP photographs.

4.5. Final Note On Method

[24] We include an important note on the generalized applicability of the method. Given the parameters provided in Tables 1, 2, and 3 the only requirements for using this

Table 2. Fourier Coefficients for Poleward Oval Boundary $\overline{PB}$ as a Function of Substorm Time[a]

Time Stamp	H_0^R	H_1^R	H_1^I	H_2^R	H_2^I	H_3^R	H_3^I	H_4^R	H_4^I	σ
T = −20 min	74.02	−4.28	−0.43	−0.55	−0.17	0.48	−0.12	0.17	0.26	0.24
T = −15 min	73.88	−4.24	−0.44	−0.61	−0.04	0.29	−0.10			0.26
T = −10 min	73.69	−4.39	−0.55	−0.57	−0.01	0.37	−0.16	0.22	0.19	0.23
T = −5 min	73.52	−4.34	−0.28	−0.69	−0.17	0.38	−0.13	0.20	0.11	0.23
T = 0.0	73.28	−4.38	−0.49	−0.65	−0.11	0.37	−0.24			0.22
T = 0.5	73.44	−3.27	−0.82	0.68	−0.67	1.03	−0.73	0.53	−0.17	0.24
T = 1.0	73.90	−1.88	−1.27	1.86	−0.61	1.37	−0.44	0.38	−0.05	0.26
T = 1.5	74.23	−1.56	−1.16	1.92	−0.45	0.94	−0.15	−0.01	0.10	0.33
T = 2.0	74.61	−1.68	−0.96	1.55	−0.30	0.86	−0.06	−0.22	0.08	0.27
T = 2.5	74.71	−1.71	−0.74	1.10	−0.33	0.76	0.05			0.30
T = 3.0	74.66	−1.78	−0.68	1.02	−0.53	0.65	0.10	−0.08	0.22	0.27

[a]The standard deviation in degrees (σ) between the Fourier fit and the average location is indicated in the last column.

Table 3. Fourier Coefficients for Equatorward Boundary $\overline{EB}$ in the Same Format as Table 2

Time Stamp	H_0^R	H_1^R	H_1^I	H_2^R	H_2^I	H_3^R	H_3^I	H_4^R	H_4^I	σ
T = −20 min	68.84	−5.58	−1.99	0.42	0.30					0.25
T = −15 min	68.78	−5.75	−1.74	0.23	0.32					0.25
T = −10 min	68.69	−5.88	−1.66	0.54	0.07	0.08	0.32			0.25
T = −5 min	68.69	−6.13	−1.49	0.63	0.07	−0.06	0.41	0.03	−0.27	0.24
T = 0.0	68.43	−5.80	−1.69	0.42	0.27	0.00	0.46			0.26
T = 0.5	68.13	−6.17	−1.49	0.63	0.15					0.29
T = 1.0	68.21	−6.68	−1.40	0.86	−0.05					0.27
T = 1.5	68.13	−6.89	−1.80	1.11	0.00	−0.25	0.04	−0.22	−0.23	0.23
T = 2.0	68.32	−6.77	−1.59	0.94	−0.23					0.28
T = 2.5	68.82	−6.87	−1.71	0.58	−0.41	0.13	0.17	−0.30	−0.10	0.25
T = 3.0	68.92	−6.65	−1.81	0.67	−0.26	−0.07	0.11			0.23

normalization method is an auroral image for which the entire bulge is identifiable and the time of the image in normalized substorm time. The pixel locations of the image can then be normalized to positions in our average substorm. Hence a superimposed epoch analysis could be performed with any type of data with known positions acquired at the same time as the images. The technique is not limited to relative auroral intensity but could be applied to any data set obtained simultaneously by ground based or satellite borne instruments such as ground magnetic field perturbations, convection electric field, and neutral wind.

[25] Without these normalizations the results of superimposed epoch analyses will give smeared and/or misleading results. Shortly into an event, normalizing only to onset time rather than our substorm time will mix data from the recovery period with the expansion period. Without the spatial normalization, data from different parts of the substorm will unquestionably be mixed together.

4.6. An Application of the Normalization Results

[26] We now apply our normalization technique to determine the average UV emission patterns as a function of substorm phase using all 116 events. The position of each pixel in an image is normalized to a pixel in our average substorm and then all the intensities in the normalized pixel are averaged. Figure 4 shows the average patterns for the 11 time steps of the classical auroral substorm as observed by the Polar VIS Earth Camera. The localized onset is centered at 22.4 MLT and 66.7° Ilat. The characteristic poleward expansion of the oval is accompanied by eastward and westward expansions. During expansion the poleward boundary of the bulge is nearly a straight line. The maximum extent of poleward expansion remains at approximately the MLT of the onset. The entire pattern is asymmetric around midnight. The most intense emissions are found in the western and poleward part of the bulge. As will become more apparent later in the paper, another region of intensified emissions remains within the original oval, offset to the east. Thus the key features of the individual events are maintained in the normalized substorm.

5. Validation of Methodology

[27] We will now perform a quantitative validation of the normalization technique using the average emission patterns just compiled. The validation will be done in two steps: (1) we will evaluate the final average patterns deduced from all events (shown in Figure 3); and (2) as an illustration we will deduce average patterns for the two example events shown in Figure 1.

5.1. All Events

[28] We address the performance of the normalization scheme by calculating the correlation coefficient between each individual event and the average pattern. For each event the count in a specific pixel is plotted as a function of the counts in the same location in the average pattern and the resulting scatterplot is used to determine the correlation coefficient. This is done for each of the three levels of normalization, for each of the 116 events and for each of the 11 time steps. As an example Figure 5 shows histograms of the correlation coefficients for T = 1.0 and all three levels of normalization. Note the clear improvement of the performance as each normalization is introduced and the rather impressive fact that none of our 116 events has a correlation coefficient lower than 0.75. This is remarkable considering the high variability of the emission patterns of the substorms. Table 4 lists the median correlation coefficients for all 116 events at each time step. Note that the correlation coefficient at the peak of the substorm (T = 1.0) is 0.89 indicating that the average pattern shown in Figure 4 represents the individual events while the low standard deviation of only 0.04 indicates that it represents virtually all of our 116 events. As discussed earlier a selection criterion for the events required an expansion from a local onset, and we found that the expansions resulted in the bulge-type auroral substorm. Hence it is expected that the highest correlation coefficients would be seen during the expansion phase, peak, and early recovery phase when this feature is dominant. Later in the recovery phase when the bulge is fading the correlation coefficient decreases accordingly. We next question the statistical variation of the patterns by asking: What is the standard deviation to the average patterns? For the peak of the substorm Figure 6 shows the standard deviation relative to the counts in the average pattern (Figure 4) for counts greater than or equal to 10. The standard deviation is roughly 30–60% of the average count. This is not insignificant. Hence there is a considerable deviation between the intensities in the individual events and the average pattern. This is, however, not a contradiction to the conclusion based on Table 4 that the average pattern indeed represents our 116 events. Comparing the high correlation and small standard deviation of Table 4 with the considerable variation in Figure 6 simply means that while features seen in our average patterns represent the emission pattern of the individual event they

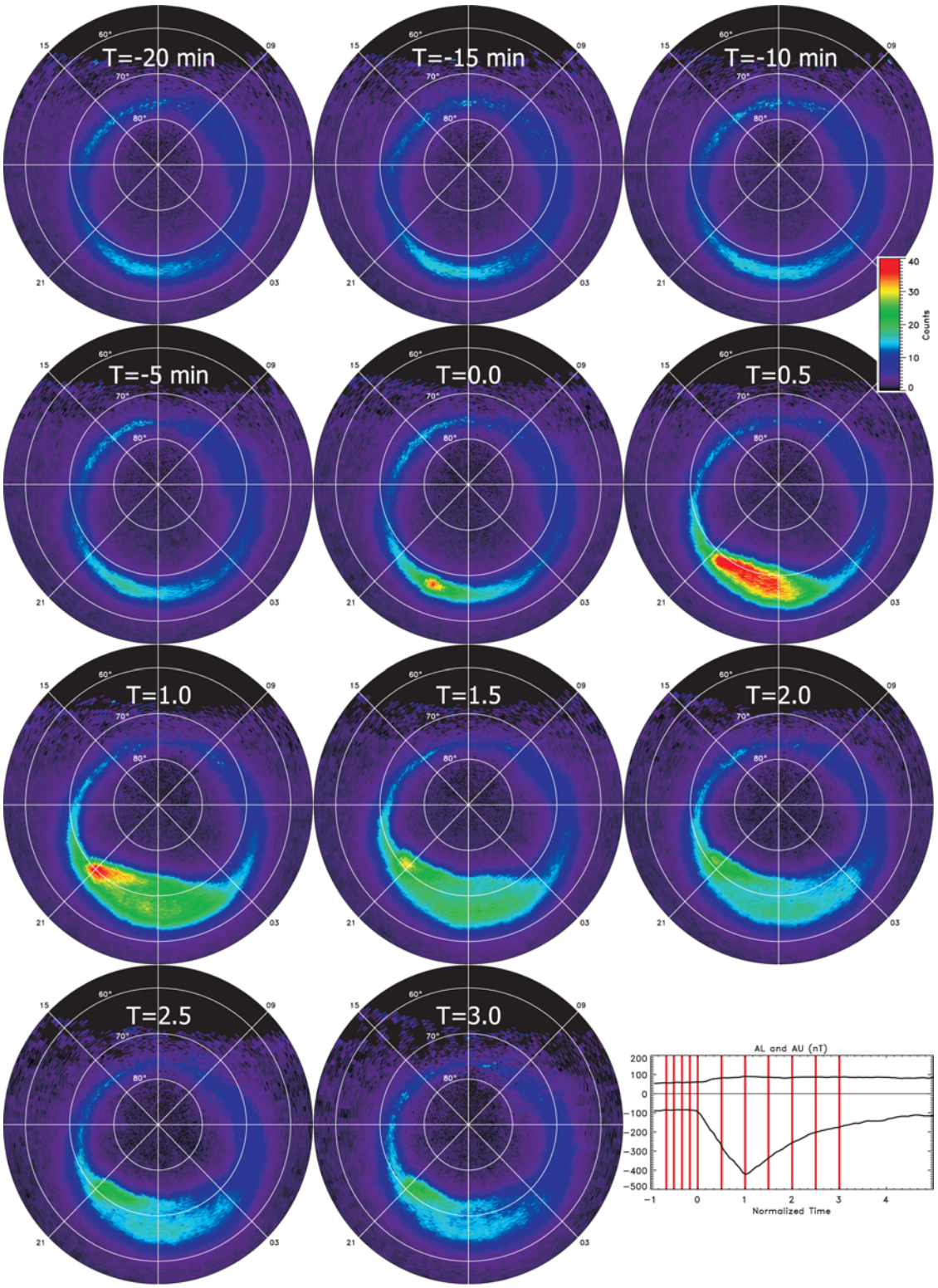

Figure 4. Average UV auroral ovals at 11 time steps of a substorm after normalization in substorm time, local time, and latitude.

do not necessarily represent the intensity. Figures 1h and 1k illustrate this point.

[29] We have not performed any normalization by substorm intensity. There is no separation according to the intensity of the westward auroral electrojet (for example as measured by AL) or by the UV emission intensities. Substorms reaching −1000 nT are mixed with substorms reaching only −200 nT. Nevertheless, Table 4 clearly shows that

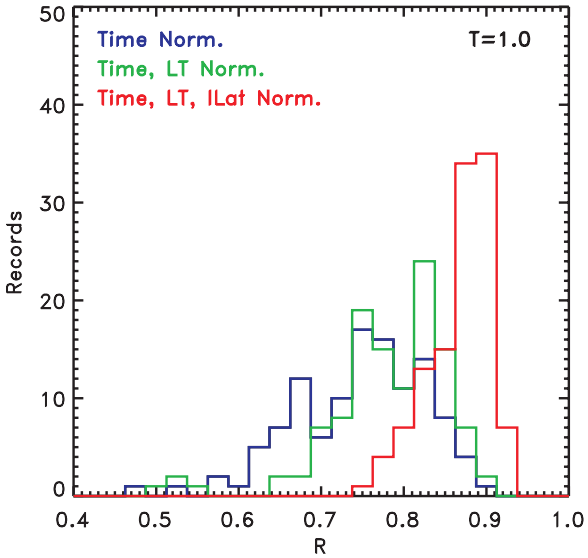

Figure 5. Histograms of the correlation coefficients between the individual events and the average pattern shown in Figure 4 for the time step T = 1.0. All three levels of normalization are shown, which clearly illustrates the value of each normalization step.

these two parameters have little or no effect on the relative emission patterns and they are all well represented by our average emission patterns.

5.2. Two Example Events

[30] Returning to the two events shown in Figure 1, we can quantify the performance of the normalization technique. Determining an average auroral emission pattern using only the substorm time normalization (step 1) we find obvious artifacts as seen in Figure 1c. For example the surge heads are not positioned in the same location and hence the average patterns consist of two washed out surge heads. The scatterplots of the counts in each image (Figures 1a and 1b) to the average pattern (Figure 1c) are shown in Figures 1f and 1i, where the correlation coefficients are 0.80 and 0.92, respectively. Of course the more intense event correlates better with the average. Performing both temporal and local time normalization (steps 1 and 2), the average of the two example events is shown in Figure 1d. While the average looks more like a classical substorm, the surge head is not bright and the poleward boundary is not straight as seen in both events individually. The correlation coefficients are roughly unchanged 0.82 and 0.92, respectively, though slightly improved for the weaker event.

[31] Finally, Figure 1e shows the average of the two events using all three steps in the normalization scheme. Clearly, the characteristics of the individual events are maintained to a higher degree than in Figures 1c and 1d. We find that the correlation coefficients (Figures 1h and 1k) are improved to 0.93 and 0.97, with the weaker event now much better correlated.

[32] In summary we can conclude that even though the individual events may vary significantly in intensity, size, position, and lifetime they all have key emission features and can be represented by our average pattern seen in Figure 4. Thus our normalization results quantitatively validate the Akasofu assumption mentioned in the introduction.

6. Analysis of the Average UV Emission Pattern

[33] Previously, *Gjerloev et al.* [2007] had quantified the spatiotemporal behavior of several key emission features of the classical substorm, using the same set of substorms as this study. They carefully identified visually in each image the location and movements of these key features and concluded that the two components separate in latitude and offset in MLT, although they observed some optical connections in the MLT interval of overlap. Using the same set of substorms, we applied our new normalization technique to determine average UV emission patterns as a function of substorm phase (Figures 4). We noted that the maximum emission intensities appeared in the bulge, but another region of enhanced emissions developed at the latitudes of the original oval but offset to the east of the onset MLT. Thus both approaches came to the same conclusion that the substorm portion of the auroral oval bifurcated during the expansion phase. We will now analyze this bifurcation in detail.

[34] We analyze the emission patterns of Figure 4 by fitting a single or double Gaussian as needed to the latitudinal intensity distributions at 24 magnetic local times for each time step of the substorm. The function we fit is

$$f(ILat) = A_1 \exp\left(-(ILat - A_2)^2/A_3\right) + A_4 \exp\left(-(ILat - A_5)^2/A_6\right) + A_7 \quad (5)$$

We use a nonlinear least squares Levenberg-Marquardt algorithm to determine the parameters, A_{1-7}, at each of the 24 local times. Figure 7 shows the results of our fits for T =

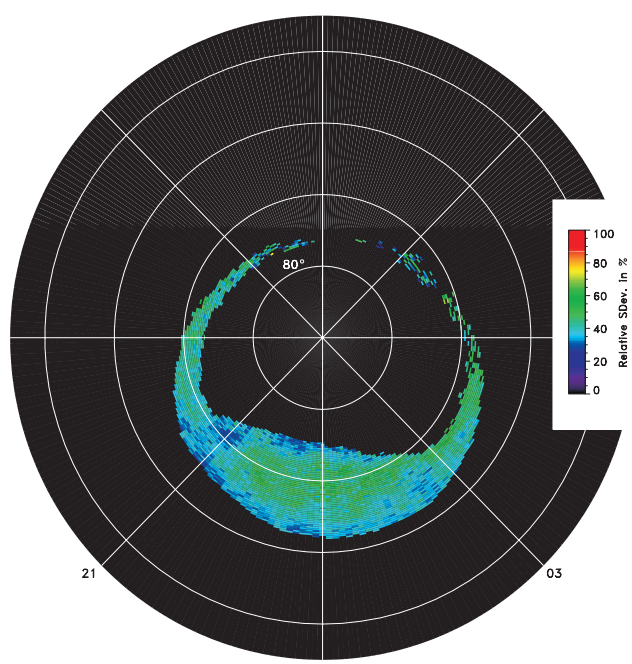

Figure 6. Relative standard deviation of the average emission pattern for T = 1.0.

Table 4. Median Correlation Coefficient Between Average Patterns and All Individual Events[a]

	Normalization		
Time Stamp	Temporal	Temporal and Local Time	Temporal and Local Time and Latitudinal
T = −20 min	0.60 ± 0.12	0.59 ± 0.12	0.70 ± 0.10
T = −15 min	0.60 ± 0.12	0.59 ± 0.12	0.72 ± 0.10
T = −10 min	0.61 ± 0.12	0.61 ± 0.12	0.72 ± 0.11
T = −5 min	0.62 ± 0.12	0.61 ± 0.12	0.73 ± 0.10
T = 0.0	0.64 ± 0.10	0.65 ± 0.11	0.79 ± 0.07
T = 0.5	0.75 ± 0.10	0.79 ± 0.10	0.88 ± 0.05
T = 1.0	0.77 ± 0.08	0.80 ± 0.07	0.89 ± 0.04
T = 1.5	0.74 ± 0.08	0.77 ± 0.08	0.86 ± 0.06
T = 2.0	0.71 ± 0.08	0.76 ± 0.08	0.84 ± 0.06
T = 2.5	0.69 ± 0.10	0.73 ± 0.09	0.81 ± 0.07
T = 3.0	0.69 ± 0.09	0.71 ± 0.10	0.81 ± 0.08

[a]Standard deviation to the median is also indicated. Three different levels of normalization are used.

1.0, and disregarding the uninteresting offset A_7 (median offset is ∼1.6), the function is given within each MLT bin along with the correlation coefficient. The black line shows the cross section of the oval while the red line shows the fit. Outside the bulge, a single Gaussian is sufficient to reproduce the latitudinal profiles but within the bulge the emissions resemble double, though overlapping, Gaussians. Note the extremely high correlation coefficients, equal to or exceeding 0.97 for the entire nightside. Also note that for MLTs of 22.4 to 0.4 the data peak sharply on the poleward side of the Gaussian maxima and drop to the polar cap values slightly faster than the Gaussian can follow. Such a sharp emission characteristic can only be maintained by using a normalization in latitude.

[35] Figure 8 summarizes the results of the Gaussian fits at all eleven time steps. In column 1 is shown the data from Figure 4. For comparison with the 24 Gaussian fits the data plots are deduced from latitudinal cuts at MLTs = 0.4, 1.4, 2.4. . .22.4 and 23.4 (hours in MLT from the onset MLT) as in Figure 7. Column 2 shows the Gaussian fits with the correlation coefficients. Linear interpolation is used between hourly profiles for both data and fits. Note the exceptional similarity between the data and the fits. Columns 3 and 4 show the two individual Gaussian components separately. It is remarkable, first, that a simple single or double Gaussian is able to reproduce the auroral emission distributions for all MLTs and time steps, and second, with a correlation coefficient in every case of ≥0.97.

[36] The temporal behavior of the two Gaussian components (columns 3 and 4) is very different. While the bulge changes in latitudinal position, local time extent and amplitude, rising (in latitude) and expanding out of the original auroral oval, the oval aurora only changes amplitude along the original oval. The onset occurs within the original oval at which time the two distributions are completely overlapping. It is of interest that the fit identifies onset at 66.8° as was found statistically by *Gjerloev et al.* [2007] using a completely different method.

[37] The apparent differences in spatiotemporal behavior between the two components are illustrated more quantitatively in Figures 9 and 10. The first figure shows separately the two Gaussian fits at five local times from 21.4 MLT to 1.4 MLT for the time steps T = 0.0 to T = 3.0. Note that the Bulge aurora does not exist at all local times for all time steps (for example T = 0.0 at MLT = 21.4). The bulge fits have pronounced substorm time dependence, rising from zero and expanding both poleward and in local time both

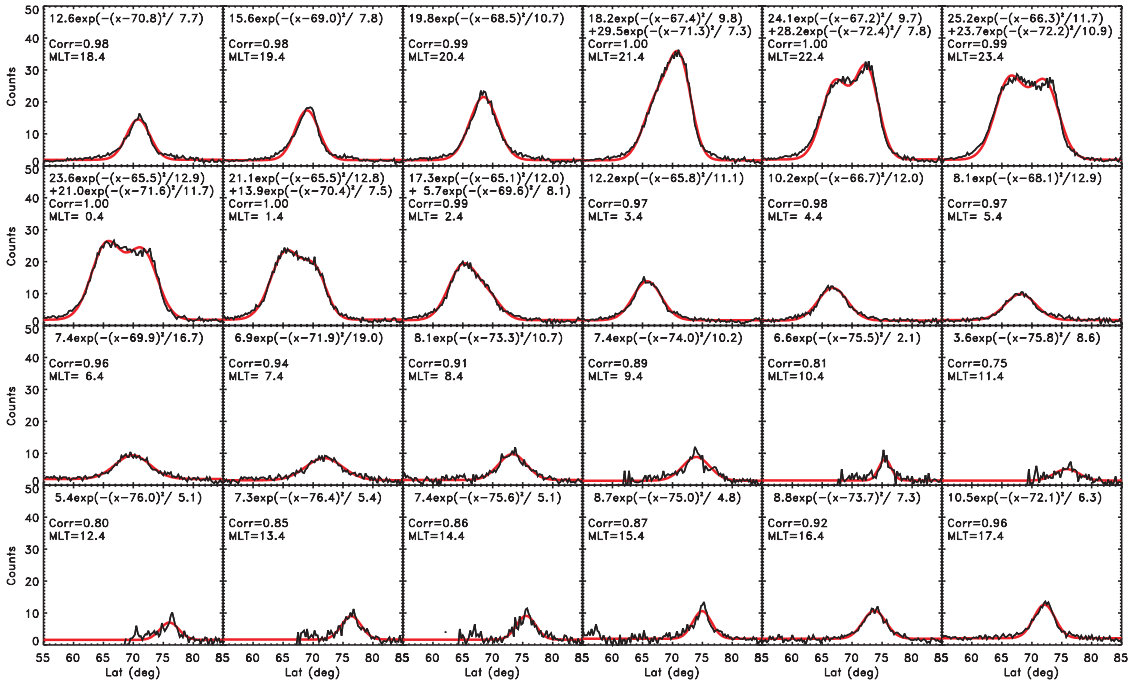

Figure 7. Latitudinal profiles of the average peak oval shown in Figure 4 for 24 magnetic local times (black) and Gaussian fits (red). Note average onset is 22.4. MLT Corr indicates the correlation coefficient between data and fit.

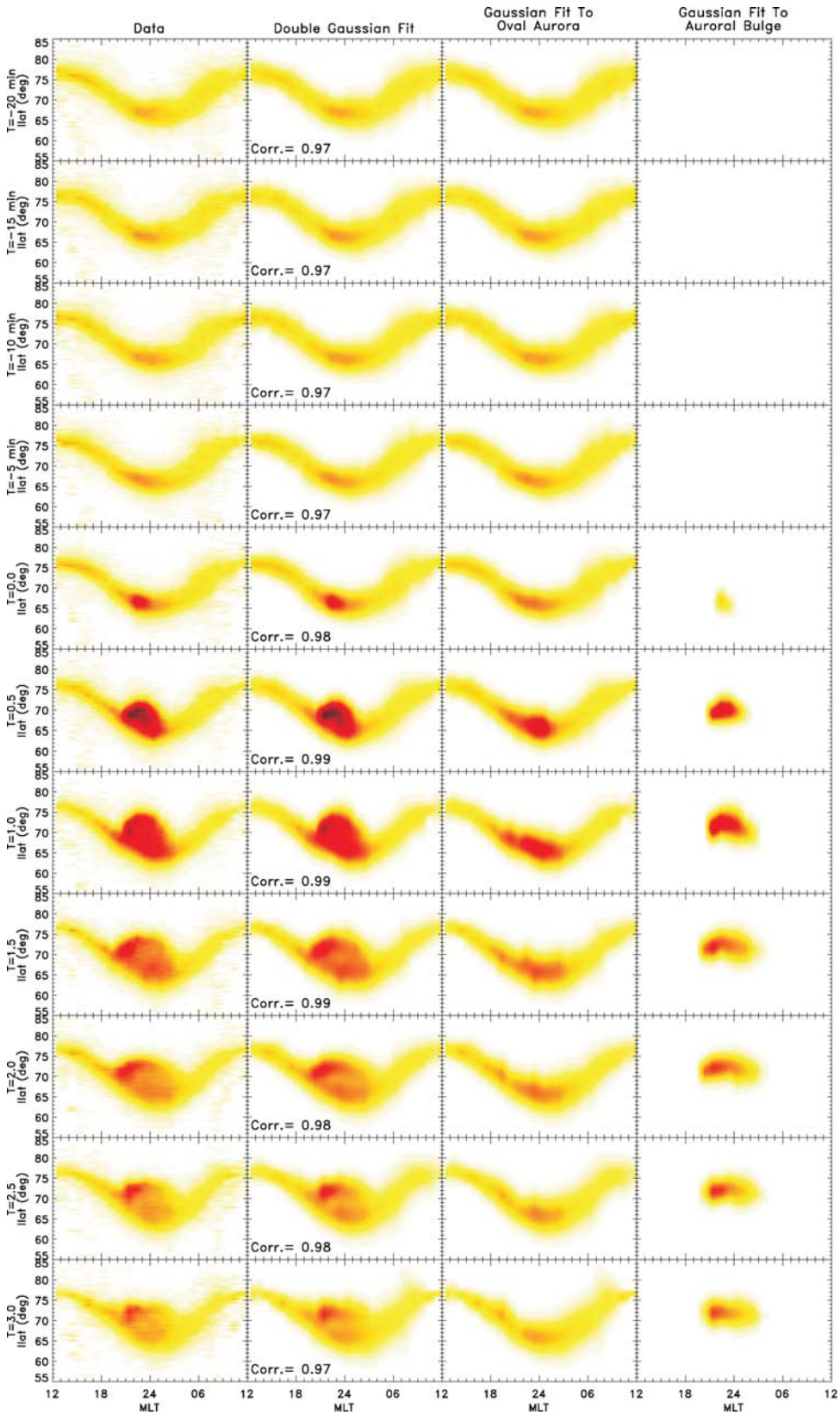

Figure 8. Columns show the average ovals (see Figure 4), ovals from a double Gaussian fit, the oval auroral Gaussian fit component, the bulge Gaussian fit component, and the oval aurora Gaussian fit with the preoval intensity subtracted. Corr indicates the correlation coefficient between columns 1 and 2.

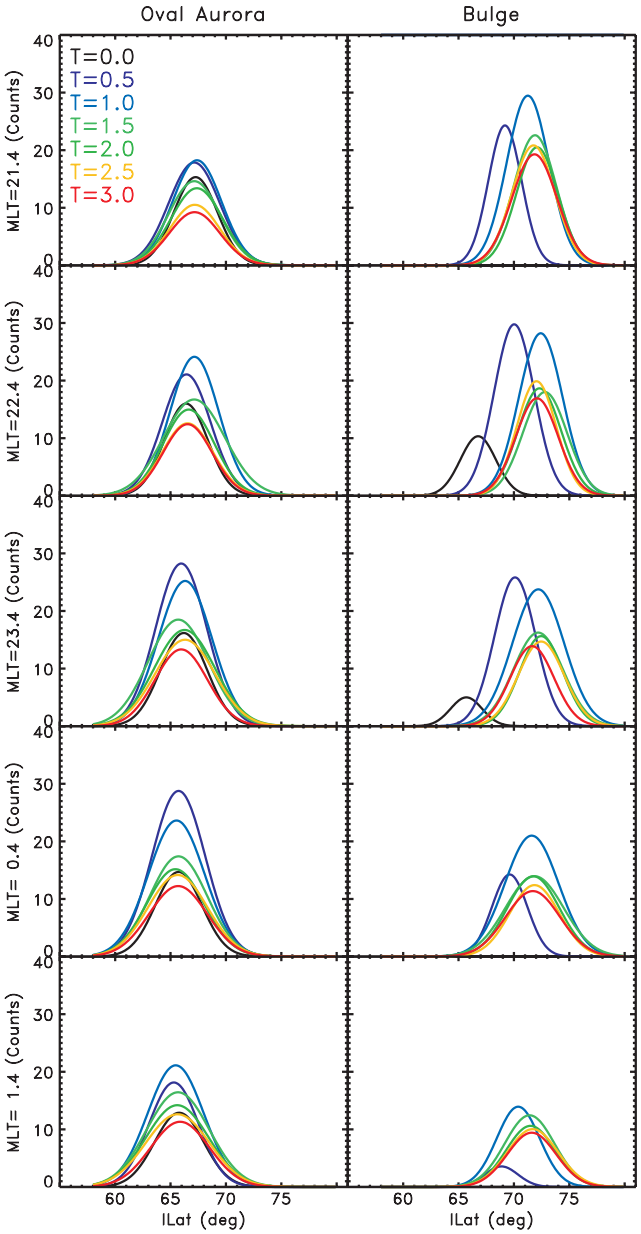

Figure 9. Gaussian fits to the two separable oval components at five local times and seven time steps.

west and east. *Gjerloev et al.* [2007] showed that the amount of expansion west and east were, on the average, about equal. The location in MLT of the maximum poleward expansion of the Gaussian peak remains very close to the MLT where the onset occurs (22.4 MLT), just as we found that the maximum poleward expansion of the boundary remains very close to this MLT [*Gjerloev et al.*, 2007]. The peaks then remain quite stationary in latitude during the recovery period. In contrast to the bulge aurora, the peak intensities of the oval aurora Gaussians increase by only 50% above preonset values, maximize before the substorm maximum, and more quickly decay to the preonset values. This is better seen in Figure 10, which shows the intensities at the peaks of each Gaussian (A_1 and A_4) as a function of MLT for each of the time steps from onset. However, the maximum values of the oval aurora Gaussians do reach intensities comparable to the bulge values (compare at T = 1 the black and green plots in Figure 10). The oval aurora enhancement over its preonset values occurs at later local times than onset, around midnight or slightly after. By 3.4 MLT there is little evidence of any substorm activity.

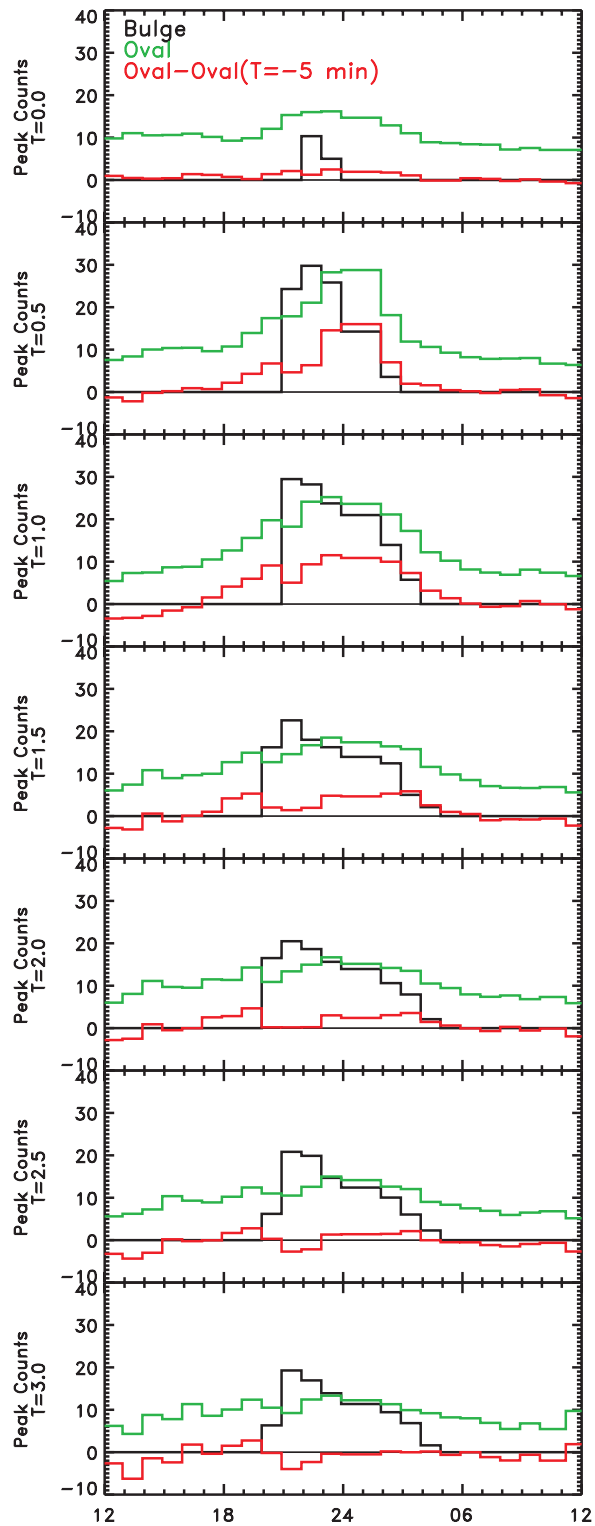

Figure 10. Peak values of the Gaussian fits as a function of MLT; black is bulge aurora, green is oval aurora, and red is oval aurora minus the presubstorm value.

Especially note the difference between the bulge intensity (black) and the oval intensity with the preonset oval removed (red) that shows the 2-h offset in MLT of the two components and the rapid decay of the oval aurora to even below onset intensities. Because of these differences in their temporal and spatial behavior, we conclude that the bulge aurora and oval aurora are quasi independent. This conclusion and its implications will be further discussed in the next section.

7. Discussion

7.1. Limitations to Approach

[38] Despite over 40 years of substorm research, the hand-drawn phenomenological patterns of *Akasofu* [1964] remain the only reference to what an optical substorm looks like. The contemporary study by *Feldstein* [1963] also used all-sky camera images from the IGY (1957–1958) to determine the location and width of the auroral belt as a function of magnetic activity, but his study was not substorm related. Subsequently, numerous event studies have investigated individual features of the optical substorm. This lack of progress in quantifying the global substorm characteristics is certainly remarkable considering the vast amount of global auroral images obtained by various space-borne imagers. However, any derivation of the global auroral substorm from space-borne imagers will necessarily yield a different perspective of the substorm than one derived from all-sky cameras, since the latter have much higher spatial resolution that can indicate the type of auroral structure existing in the various parts of the substorm. The imager obtains an average intensity over the size of a pixel, typically ~70 km in diameter, but with higher sensitivity than the all-sky camera pictures. Thus for relatively unstructured aurora it is more sensitive. However, the opposite occurs for structured aurora because of the averaging characteristics of the imager over the area of a pixel. However, all-sky cameras cannot provide a cohesive indication of the relative global-scale intensity distribution and structures that should be derivable from global images. Thus we have concentrated on the global characteristics of the substorm emissions.

[39] In this paper we have intentionally used the counting rates provided by the VIS Earth Camera, an imager having a broad spectral response, since it was designed as an engineering camera for control of the two visible imagers [*Frank et al.*, 1995]. It has been shown that the ultraviolet aurora is produced by electrons primarily in the kilovolt energy range [*Germany et al.*, 1997], similar to the visible aurora in unfiltered all-sky camera pictures. This energy range is most appropriate for detecting the distribution of the main electron precipitation associated with the substorm aurora. However, the typical energy of precipitating electrons in the surge region often exceeds 10 keV [e.g., *Fujii et al.*, 1994, Figure 5; *Weimer et al.*, 1994, Figure 4], while during the recovery phase the high-latitude postmidnight aurora contains considerable fine structure of sub-keV electrons that extends to high latitudes [*Fujii et al.*, 1994, Figure 8]. High-energy electrons, detected through their X-ray bremsstrahlung [*Østgaard et al.*, 1999] are also found to drift into the morning hours. Thus our results may underestimate the relative intensity of the auroras in these regions. For these and other reasons we have deliberately not converted the counting rates to emission intensities or energy flux as has been done in previous papers [e.g., *Newell et al.*, 2001]. For this time period the brightness in kR of the aurora within the wavelength interval of measurement could be estimated by the relationship: I(kR) = N/4.3, where N is the flat field digital number ("dn" or counts observed by the instrument in each pixel) and the intensity, I, is measured in kilorayleighs, assuming that the majority of the signal is from the atomic OI emissions at 130.4 and 135.6 nm. Since we only observe the emissions at a single wavelength (interval) we cannot calculate the energy flux without making a number of further assumptions [see, e.g., *Germany et al.*, 1997]. However, we prefer to maintain the unit of "counts" in our plots so as not to mislead the reader regarding the capabilities of the measurement.

[40] In producing the average patterns, however, we have made a number of assumptions that should be acknowledged, all resulting in loss of spatial or temporal resolution. (1) The imager counts are column-integrated measurements from columns not parallel to the magnetic field, hence are aspect dependent. (2) The finite exposure time will average temporal variations. (3) A known property of CCD based images is bleeding or cross contamination between neighboring pixels. (4) The spatial size of the individual pixels at ionospheric altitudes varies with the altitude of the spacecraft and image aspect. (5) The normalization technique distorts the pixel sizes from the original measurements without adjusting the intensities. (6) The normalization technique does not normalize the two components independently and hence does not account for differences in the local time overlap between the two components. Despite these issues that all lead to smearing and hence affect the shapes of the latitudinal profiles, the results presented in the validation section, Figure 4, and shown in Table 4 do validate our technique.

7.2. Use of Gaussians

[41] The idea of a two-component optical auroral oval was first made by *Elphinstone et al.* [1995a, 1995b] who referred to the double oval as a distribution that forms at the beginning of the substorm recovery phase. *Carbury et al.* [2003] fitted a function consisting of a single Gaussian plus a second order polynomial [see also *Eastes et al.*, 2000], although they pointed out that not all auroral latitude profiles could be fitted with a function based on a single Gaussian. Then *Mende et al.* [2003] published an interesting study in which they performed a superposed epoch analysis of 91 substorms using data obtained from the IMAGE spacecraft. They fitted a function consisting of two Gaussians and a linear function to the auroral intensity latitudinal profiles (imager counts) for each substorm individually from which they primarily obtained boundary locations. However, they conceptually viewed the oval as a single distribution having the shape of a double Gaussian and never interpreted the two Gaussians as separate entities. In contrast to all previous uses of Gaussians to describe the intensity distributions of the substorm aurora, we argue that they represent individual components and subsequently analyze the spatiotemporal behavior of these two components separately.

Table 5. Comparisons of the Locations of Auroral Boundaries at the Local Time of Onset[a]

	This Paper		*Gjerloev et al.* [2007]		*Mende et al.* [2003]		*Akasofu* [1994]
Time	Poleward	Equator-ward	Poleward	Equator-ward	Poleward	Equator-ward	Poleward
0.0	69.5	63.5	68.7	64.0	67.2	61.6	67.2
0.5	73.0	63.5	71.7	63.4	70.8	61.6	71.7
1.0	75.5	63.5	74.0	63.6	71.5	61.7	77.1
1.5	75.5	63.5	73.8	63.6	71.7	61.9	71.1
2.0	75.0	63.5	73.5	63.9	72.0	62.7	
2.5	74.5	64.0	73.0	64.1	72.7	62.8	69.0
3.0	74.5	64.0	73.3	63.9	73.1	62.5	

[a]Data in the *Mende et al.* [2003] column are obtained from their Figure 8 and data in the *Akasofu* [1994] column are from his Figure 8.

7.3. Boundary Comparisons

[42] We have three independent statistical studies of the average poleward and equatorial boundary locations as a function of substorm time that can be compared: (1) average locations from histogram distributions obtained by a manual estimation of the boundary locations from individual images [*Gjerloev et al.*, 2007]; (2) average locations from an automated boundary program (this study, Figure 3); (3) locations averaged from double Gaussian fits to latitude profiles of auroral intensities [*Mende et al.*, 2003].

[43] Comparisons can be made only at the onset MLT, since that is the only common MLT used in the three analyzes. Substorm time was scaled using the same normalization procedure for the first two methods. For the *Mende et al.* [2003] boundaries we assumed 30 min as a timescaling factor T = 1.0). While the *Akasofu* [1964] diagrams are schematic models, it is of interest to scale the drawings for comparison. We use midnight in his latest diagrams [*Akasofu*, 1994] where the poleward boundary is more clearly defined than in previous publications but not his equatorward boundary, which remains vague. For times we use his diagram B (0 $\sim$ 5 min) for T = 0, C (5–10 min) for T = 0.5, D (10–30 min) for T = 1.0, E (30 min to 1 h) for T = 1.5 and F (1–2 h) for T = 2.5.

[44] The comparisons are shown in Table 5. In all three cases the general boundary motions are similar, with the poleward boundary increasing by about 5° to T = 1.0 but the equatorward boundary staying relatively stationary. The Akasofu diagrams show much more dynamics, with a poleward motion of about 10°, reaching higher latitude than the three statistical methods. After the substorm maximum, the first two methods show a small retraction of the poleward boundary, while the method 3 boundary continues to increase. This is probably due to the lack of substorm time normalization for which the slower developing substorms are still expanding after T = 1.0. The Akasofu diagrams show a large, rapid retraction.

[45] The relative motion of the boundaries between methods 1 and 2 is very similar, although there is a systematic offset of +1.5° in the poleward boundary while no difference is seen in the equatorward boundary. One can conclude that the typical intensity at the boundary for method 2 was slightly larger than for method 1. While the general progression of the *Mende et al.* [2003] boundaries is similar, the offsets are large but not as constant for both the poleward and equatorward boundaries. Since the signs of the offsets are the same for both boundaries, the differences cannot be attributed to different intensity selections. The only other systematic difference between the method used in 3 and the method of 2 would be the registration of the pixels on the Earth. If the registration difference were approximately 2° (the average of the poleward and equatorward differences), then the additional poleward difference of −0.5° and equatorward difference of +0.5° could be attributed to an average higher intensity used by the method 3 to define the boundary location. Thus the average oval width at the time of the peak and at the onset local time is larger from method 1 than either 2 and 3 by over 1°, reaching 12.0°, 10.4°, and 9.8° for the three methods, respectively.

7.4. Implications

[46] We have performed two independent analyses of the characteristics of auroral substorms. From our previous article [*Gjerloev et al.*, 2007] and this article we now have quantitative measurements of bulge-type auroral substorms, both for an average substorm and distributions of the locations and rates of expansion of key features of these substorms. We have also come to the same conclusion that the optical emissions separate during the expansion phase of a substorm into two components that are quasi-independent. They show independence because of the differences in their behavior spatially and temporally:

[47] 1. The bulge aurora starts with a localized onset, that is, a new region of emissions within the preonset oval, whereas the oval aurora brightens simultaneously within the preonset oval over some hours in local time. This implies that two different electron precipitation and energization sources exist in the magnetosphere. The initial brightening within a region of preexisting auroral arcs is well documented [e.g., *Akasofu*, 1964; *Lui and Burrows*, 1978; *Shepherd and Murphree*, 1991]. However, the characteristics of the large-scale brightening of the oval aurora are not well documented.

[48] 2. The bulge aurora expands poleward out of the presubstorm oval as well as westward and eastward from the premidnight onset location with comparable distances on the average (see *Gjerloev et al.* [2007] for additional quantitative descriptions of the expansion and its speeds), whereas the oval aurora brightens almost entirely to the east of the onset location. This results in a very asymmetric total emission pattern around midnight. Thus during this period there is a separation of the precipitation/energization regions.

[49] 3. The oval aurora emissions decay more rapidly than the bulge emissions, nearly settling to preonset levels by T = 2.0 (30 min into the recovery phase). Thus the decays have separate time constants, again indicating sep-

arate precipitation mechanisms. This contrasts the *Chua et al.* [2004] analysis that assumed a single time constant to determine the decay of the aurora brightness thereby implying that the entire substorm behaves as a single component system.

[50] On the other hand, we cannot say that the two emission regions are totally independent because the onsets of their rapid intensifications occur simultaneously and some auroral forms are seen to connect the two regions in the MLT interval of overlap [*Partamies et al.*, 2006]. From these observations we conclude that while the two emission regions are parts of the same phenomenon, the precipitation and energization mechanisms of electrons producing the emissions must be different.

[51] We have no direct method of determining the magnetospheric source regions of the precipitating electrons producing the observed emissions since the broadband UV measurements yield no specific differentiations on the various characteristics of the precipitating electrons. While many articles have been published that do relate electron measurements to specific auroral forms (e.g., see comments and references in section 7.1 and the systematic study of electrodynamic parameters during substorms by *Fujii et al.* [1994]), the study by *Gjerloev and Hoffman* [2000a, 2000b] is of special interest. They deduced an empirical model of the nightside height-integrated ionospheric conductivity during the expansion phase through early recovery phase of a classical bulge type substorm using measurements of precipitating electrons. They found two enhanced conductance channels within the substorm bulge aurora overlapping in local time but separated in latitude. The similarities with our bifurcated oval are striking. Since their model was based on measured electron precipitation, they were able to identify the magnetospheric origins of the channels (following *Winningham et al.* [1975]) and concluded that they were produced by electrons originating from the boundary plasma sheet (premidnight, high-latitude channel) and the central plasma sheet (postmidnight, low-latitude), respectively. However, such general identifications do not provide explanations of the spatial and temporal morphology of the two components of the auroral substorm, especially the differences in local time of the enhancements.

8. Summary and Conclusions

[52] Using global auroral images obtained by Polar VIS Earth Camera we have analyzed the UV emission patterns from 116 fairly isolated auroral substorms. We found that essentially all isolated auroral events that originate from a localized onset expand into the Akasofu bulge-type aurora.

[53] We then compiled average auroral emission patterns for 11 time steps of the substorm covering 20 min prior to the onset until well into the recovery phase. The high variability of the substorm lifetime as well as large variability in the position and size of the auroral bulge presented a complication for deducing average or superimposed epoch patterns. We obtained these patterns using a unique three-step normalization technique, one temporal based on the expansion time of the substorm, and two spatial, magnetic local time and latitude. The normalization technique is shown to be highly effective in maintaining the key features in the individual auroral emission patterns. Histograms of the correlation coefficients between the individual events and the average pattern show high coefficients and small standard deviations, indicating that the average pattern well represents the individual events while the low standard deviation indicates that they represent virtually all of our 116 events. Thus our normalization results quantitatively validate the *Akasofu* [1964] assumption that key auroral features exist in the bulge-type auroral substorm.

[54] The normalization technique is not limited to relative auroral intensity but could be applied to any data set obtained from ground-based or satellite-borne instruments simultaneously with an auroral image for which the entire bulge is identifiable.

[55] These average patterns were well fit to either a single or double Gaussian distribution in latitude for each of 24 magnetic local times. On the basis of our analysis of the normalized average substorm and the temporal/spatial behavior of these Gaussians, we made the following conclusions. The bulge aurora starts with a localized onset, a new region of emissions within the preonset oval, whereas the oval aurora brightens simultaneously within the preonset oval over some hours in local time. This implies that two different electron precipitation and energization sources exist initially in the same region of the magnetosphere. The bulge aurora then expands poleward out of the presubstorm oval as well as westward and eastward from the premidnight onset location with comparable distances, whereas the oval aurora brightens almost entirely to the east of the onset location. This results in a very asymmetric total emission pattern on either side of midnight indicating separate the precipitation/energization regions. We further find that the decay of the oval aurora emissions and the bulge emissions have separate time constants. Owing to these pronounced differences in the spatiotemporal behavior of the two auroral components we speculate that the two components are quasi-independent, and thus their sources must also be quasi-independent.

[56] These different temporal and spatial behaviors of the bifurcated auroral substorm have implications regarding the sources of electrons that produce the emissions. The onset within the preonset oval implies that two different electron precipitation and energization mechanisms exist initially in the same region of the magnetosphere. The bifurcation of the oval during the expansion phase indicates a separation of the precipitation/energization mechanisms. The separate time constants of the decays emphasize the independence of the two sources. However, the simultaneous onset of the brightenings of both components indicates that they are parts of the same phenomenon.

[57] **Acknowledgments.** RAH acknowledges that his participation in this work was supported by contract 900894 from the Johns Hopkins University Applied Physics Laboratory and the emeritus program with the NASA Goddard Space Flight Center. JWG acknowledges NASA grants LWS02-0000-0084 and SRT02-0000-0081. JWG further acknowledges valuable assistance with the VIS database from M. R. Dvorsky. We gratefully acknowledge the efforts of the entire Polar UVI team who made the auroral images come into existence.

[58] Wolfgang Baumjohann thanks the reviewers for their assistance in evaluating this paper.

References

Akasofu, S.-I. (1964), The development of the auroral substorm, *Planet. Space Sci.*, *12*, 273–282.

Akasofu, S.-I. (1994), Past present and future substorm research, in *Proceedings of the Second International Conference on Substorms*, edited by J. Kan, J. D. Craven, and S.-I. Akasofu, pp. 13–26, Eur. Space Agency, Paris.

Brittnacher, M., M. Fillingim, and G. Parks (1999), Polar cap area and boundary motion during substorms, *J. Geophys. Res.*, *104*, 12,251–12,262.

Carbury, J. F., T. Sortirellis, P. T. Newell, and C.-I. Meng (2003), Auroral boundary correlation between UVI and DMSP, *J. Geophys. Res.*, *108*(A1), 1018, doi:10.1029/2002JA009378.

Chua, D., G. Parks, M. Brittnacher, G. Germany, and J. Spann (2004), Auroral substorm timescales: IMF and seasonal variations, *J. Geophys. Res.*, *109*, A03207, doi:10.1029/2003JA009951.

Craven, J. D., and L. A. Frank (1991), Diagnosis of auroral dynamics using global auroral imaging with emphasis on large-scale evolutions, in *Auroral Physics*, edited by C.-I. Meng, M. J. Rycroft, and L. A. Frank, pp. 273–288, Cambridge Univ. Press, New York.

Eastes, R. W., R. E. Daniell Jr., and F. J. LeBlanc (2000), Coincident ultraviolet imager and energetic particle sensor observations of the continuous electron aurora, *J. Atmos. Sol. Terr. Phys.*, *61*, 927–934.

Elphinstone, R. D., et al. (1995a), The double oval UV auroral distribution: 1. Implications for the mapping of auroral arcs, *J. Geophys. Res.*, *100*, 12,075–12,092.

Elphinstone, R. D., et al. (1995b), The double oval UV auroral distribution: 2. The most poleward arc system and the dynamics of the magnetotail, *J. Geophys. Res.*, *100*, 12,093–12,102.

Feldstein, Y. I. (1963), On morphology of auroral and magnetic disturbances at high latitudes, *Geomagn. Aeron.*, *3*, 183.

Frank, L. A., J. D. Craven, K. L. Ackerson, M. R. English, R. H. Eather, and R. L. Carovillano (1981), Global auroral imaging instrumentation for the Dynamic Explorer mission, *Space Sci. Instrum.*, *5*, 369–393.

Frank, L. A., J. B. Sigwarth, J. D. Craven, J. P. Cravens, J. S. Dolans, M. R. Dvorsky, P. K. Hardebeck, J. D. Harvey, and D. W. Muller (1995), The visible imaging-system (VIS) for the Polar spacecraft, *Space. Sci. Rev.*, *71*, 297–328.

Frey, H. H., S. B. Mende, and V. Angelopoulos (2004), Substorm onset observations by IMAGE-FUV, *J. Geophys. Res.*, *109*, A10304, doi:10.1029/2004JA010607.

Fujii, R., R. A. Hoffman, P. C. Anderson, J. D. Craven, M. Sugiura, L. A. Frank, and N. Maynard (1994), Electrodynamic parameters in the nighttime sector during auroral substorms, *J. Geophys. Res.*, *99*, 6093–6112.

Germany, G. A., G. K. Parks, M. Brittnacher, J. Cumnock, D. Lummerzheim, J. F. Spann, L. Chen, P. G. Richards, and F. J. Rich (1997), Remote determination of auroral energy characteristics during substorm activity, *Geophys. Res. Lett.*, *24*(8), 995–998.

Germany, G. A., G. K. Parks, H. Ranganath, R. Elsen, P. G. Richards, W. Swift, J. F. Spann, and M. Brittnacher (1998), Analysis of auroral morphology: Substorm precursor and onset on January 10, 1997, *Geophys. Res. Lett.*, *25*(15), 3043–3046.

Gjerloev, J. W., and R. A. Hoffman (2000a), Height-integrated conductivity in auroral substorms: 1. Data, *J. Geophys. Res.*, *105*, 215.

Gjerloev, J. W., and R. A. Hoffman (2000b), Height-integrated conductivity in auroral substorms: 2. Modeling, *J. Geophys. Res.*, *105*, 227.

Gjerloev, J. W., R. A. Hoffman, L. A. Frank, and J. B. Sigwarth (2000c), Causes of the Crescent Aurora, *Eos Trans. AGU*, *81*(48), Fall Meet. Suppl., Abstract SM11C-05.

Gjerloev, J. W., R. A. Hoffman, J. B. Sigwarth, and L. A. Frank (2007), Statistical description of the bulge-type auroral substorm in the far ultraviolet, *J. Geophys. Res.*, *112*, A07213, doi:10.1029/2006JA012189.

Holzworth, R. H., and C. I. Meng (1975), Mathematical representation of auroral oval, *Geophys. Res. Lett.*, *2*, 377–380.

Lui, A. T. Y., and J. R. Burrows (1978), On the location of auroral arcs near substorm onsets, *J. Geophys. Res*, *83*, 3342–3348.

Mende, S. B., H. U. Frey, B. J. Morsony, and T. J. Immel (2003), Statistical behavior o proton and electron auroras during substorms, *J. Geophys. Res.*, *108*(A9), 1339, doi:10.1029/2002JA009751.

Newell, P. T., K. Liou, T. Sotirelis, and C.-I. Meng (2001), Auroral precipitation power during substorms: A Polar UV imager-based superposed epoch analysis, *J. Geophys Res.*, *106*, 28,885–28,896.

Østgaard, N., J. Stadsnes, J. Bjorndal, R. R. Vondrak, S. A. Cummer, D. L. Chenette, G. K. Parks, M. J. Parks, M. J. Brittnacher, and D. L. McKenzie (1999), Global-scale electron precipitation features seen in UV and X rays during substorms, *J. Geophys. Res.*, *104*, 10,191–10,204.

Partamies, N., K. Kauristie, E. Donovan, E. Spanswick, and K. Liou (2006), Mesoscale aurora within the expansion phase bulge, *Ann. Geophys.*, *24*, 2209–2218.

Pellinen, R., T. Pulkkinen, and K. Kauristie (1994), Have we learned enough about auroral substorm morphology during the past 30 years?, in *Procedings of the Second International Conference on Substorms*, edited by J. Kan, J. D. Craven, and S.-I. Akasofu, pp. 43–48, Eur. Space Agency, Paris.

Shepherd, G. G., and J. S. Murphree (1991), Diagnosis of auroral dynamics using global auroral imaging with emphasis on localized and transient features, in *Auroral Physics*, edited by C. I. Meng, M. J. Rycroft, and L. A. Frank, p. 290, Cambridge Univ. Press, New York.

Torr, M. R., et al. (1995), A far-ultraviolet imager for the international solar-terrestrial physics mission, *Space. Sci. Rev.*, *71*, 329–383.

Weimer, D. R. (1994), Substorm time constants, *J. Geophys Res.*, *99*, 11,005–11,015.

Weimer, D. R., J. D. Craven, L. A. Frank, W. B. Hanson, N. C. Maynard, R. A. Hoffman, and J. A. Slavin (1994), Satellite measurements through the center of a substorm surge, *J. Geophys. Res.*, *99*, 23,639–23,649.

Winningham, J. D., F. Yasuhara, S.-I. Akasofu, and W. J. Heikkila (1975), The latitudinal morphology of 10 eV to 10 keV electron fluxes during magnetically quite and disturbed times in 2100–0300 MLT sector, *J. Geophys. Res.*, *80*, 3148–3171.

Zhou, X., R. J. Strangeway, P. C. Anderson, D. G. Sibeck, B. T. Tsurutani, G. Haerendel, H. U. Frey, and J. K. Arballo (2003), Shock aurora: FAST and DMSP observations, *J. Geophys. Res.*, *108*(A4), 8019, doi:10.1029/2002JA009701.

J. B. H. Baker and J. W. Gjerloev, Johns Hopkins University Applied Physics Laboratory, Laurel, MD 20723, USA. (jesper.gjerloev@jhuapl.edu)

L. A. Frank, Department of Physics and Astronomy, University of Iowa, Iowa City, IA 52242, USA.

R. A. Hoffman, Space Weather Laboratory, NASA Goddard Space Flight Center, Code 674, Greenbelt, MD 20771, USA.

J. B. Sigwarth, Division Office, Heliophysics Division, NASA Goddard Space Flight Center, Code 670, Greenbelt, MD 20771, USA.